Journal of Catalysis 460 (2026) 116984

Contents lists available at ScienceDirect

Journal of Catalysis

journal homepage: www.elsevier.com/locate/jcat

Research article

Amino-terphenyl covalent triazine polymers as visible-light heterogeneous photocatalysts for aerobic sulfoxidation and cross-dehydrogenative coupling reactions

Andrea Odoardo [a], Martina Milani [b], Alessandra Molinari [a], Lorenzo Poletti [b], Carmela De Risi [a], Stefano Caramori [a], Carmine D'Agostino [c,d], Min Hu [c], Paolo Dambruoso [e], Daniele Cortecchia [f], Graziano Di Carmine [b], Daniele Ragno [a,*], Alessandro Massi [a,*]

[a] Department of Chemical, Pharmaceutical and Agricultural Sciences, University of Ferrara, Via L. Borsari, 46 – 44121 Ferrara, Italy
[b] Department of Environmental and Prevention Sciences, University of Ferrara, Via L. Borsari, 46 – 44121 Ferrara, Italy
[c] Department of Chemical Engineering, University of Manchester, Oxford Road, Manchester M13 9PL, UK
[d] Department of Civil, Chemical, Environmental, and Materials Engineering, University of Bologna, Via Terracini, 8 – 40131 Bologna, Italy
[e] Institute for the Organic Synthesis and Photoreactivity of the Italian National Research Council, Area della Ricerca di Bologna, Via P. Gobetti, 101 – 40129 Bologna, Italy
[f] Department of Industrial Chemistry Toso Montanari, University of Bologna, Via Piero Gobetti, 85 – 40129 Bologna, Italy

ARTICLE INFO

Keywords:
Heterogeneous photocatalysis
Porous organic polymers
Covalent triazine polymers
Aerobic sulfoxidation
Cross-dehydrogenative coupling
Flow photochemistry

ABSTRACT

The synthesis of diamino-*p*-terphenyl covalent triazine polymers (**DAPT-CTPs**) is herein described by the direct nucleophilic substitution polymerization between cyanuric chloride (2,4,6-trichloro-1,3,5-triazine, **TCT**) and 4,4″-diamino-*p*-terphenyl (**DAPT**). **DAPT-CTPs** were prepared in semi-crystalline and crystalline forms as thermally stable, mesoporous materials with high photocatalytic activity in visible-light-mediated aerobic oxidation processes. The detailed photophysical characterization of **DAPT-CTPs** indicates that the incorporation of the **DAPT** unit into the triazine polymers creates an extended π-π and p-π conjugated structure beneficial to expanding the light adsorption range and elevating the excited states of the photocatalyst for the efficient generation of reactive oxygen species (ROS). Dedicated quenching experiments confirmed that photogenerated ROS can initiate sulfide-to-sulfoxide oxidations and cross-dehydrogenative couplings of glycine derivatives through electron and energy transfer mechanisms. By this strategy, a collection of added-value molecules, including non-proteinogenic α-amino acids, was obtained with high efficiency under mild and sustainable conditions. The remarkable stability of recyclable **DAPT-CTPs** was ultimately exploited for the fabrication of fixed-bed reactors, which were operated in long-term experiments for the continuous-flow production of the pharmacologically active sulfoxide Ricobendazole.

1. Introduction

Porous organic polymers (POPs) are an emerging class of advanced materials typically made up of robust carbon–nitrogen, carbon–oxygen, and carbon–carbon covalent bonds, whose presence imparts to them high thermal and chemical stability as well as insolubility and structural tunability through chemical functionalization at the molecular level for specific applications (energy storage, adsorption, sensing, catalysis, drug delivery, etc.) [1]. The well-specified 2D or 3D extended network of POPs leads to low-density, metal-free materials with permanent porosity and favorable surface area-to-volume ratios [2]. Many typologies of POPs have been developed over the last decades, and the distinction among these classes of materials, such as covalent organic frameworks (COFs) [3], hypercrosslinked polymers (HPCs) [4], conjugated microporous polymers (CMPs) [5], porous aromatic frameworks (PAFs) [6], and covalent organic polymers (COPs) [7], can be controversial at times because of their overlapping definitions. Covalent triazine polymers (CTPs) represent a distinct class of POPs [8], which are usually amorphous or semi-crystalline materials with moderate porosity; however, certain crystalline versions, known as covalent

* Corresponding authors at: Department of Chemical, Pharmaceutical and Agricultural Sciences, University of Ferrara, Via L. Borsari, 46 – 44121 Ferrara, Italy.
E-mail addresses: daniele.ragno@unife.it (D. Ragno), alessandro.massi@unife.it (A. Massi).

https://doi.org/10.1016/j.jcat.2026.116984
Received 6 March 2026; Received in revised form 18 May 2026; Accepted 19 May 2026
Available online 22 May 2026

triazine frameworks (CTFs), have also been reported [9–11]. The aromatic 1,3,5-triazine ring can be installed in CTPs using different methods, which affect the physical and structural properties of the materials produced [7]. In addition to their exceptionally high thermal and chemical stability, the abundance of nitrogen atoms leads to unique characteristics of CTPs, such as tolerance to humidity and enhanced adsorption properties, making them suitable for various applications including catalysis in water media [12–14] and as adsorbents for contaminants [15], metals [16], gaseous carbon dioxide [17,18], and oxygen [19,20]. The electron-rich 1,3,5-triazine moiety displays favorable optical and electronic properties as well [21]. These have been exploited for the synthesis of a series of triazine-based polymers as photocatalysts with the opportunity to tune the light adsorption, the band gap energy, and interfacial properties through the proper modulation of π-conjugation and material polarization by the careful design of monomers [22]. Accordingly, recent studies have demonstrated that CTPs and CTFs serve as effective heterogeneous photocatalysts, exhibiting improved charge separation and transfer, along with enhanced light harvesting capabilities in photocatalytic oxidation and solar fuel generation processes [23].

As part of our ongoing research on photocatalysis in heterogeneous [24,25] and semi-heterogeneous conditions [26], we herein describe the construction of amine-linked terphenyl-based covalent triazine polymers in semi-crystalline and crystalline forms through the direct nucleophilic substitution polymerization between cyanuric chloride (2,4,6-trichloro-1,3,5-triazine, **TCT**) and 4,4″-diamino-*p*-terphenyl (**DAPT**; Fig. 1) [8]. We envisaged that the combination of the nitrogen- and electron-rich triazine moiety with the diamino terphenyl unit, which has an extended π-π and also p-π conjugated structure, could lead to photocatalytic materials with appropriate charge separation, band gap energy, and band position to facilitate visible-light-mediated processes for oxygen or carbon dioxide utilization. Within the context of this research program, we present herein the synthesis of diamino-*p*-terphenyl covalent triazine polymers (**DAPT-CTPs**) together with their morphological, optical, electrochemical, and photophysical characterization by means of different experimental techniques and theoretical calculations. The photocatalytic activity under visible-light irradiation of **DAPT-CTPs** was evidenced by the generation of reactive oxygen species (ROS), which have been ultimately utilized to trigger selective

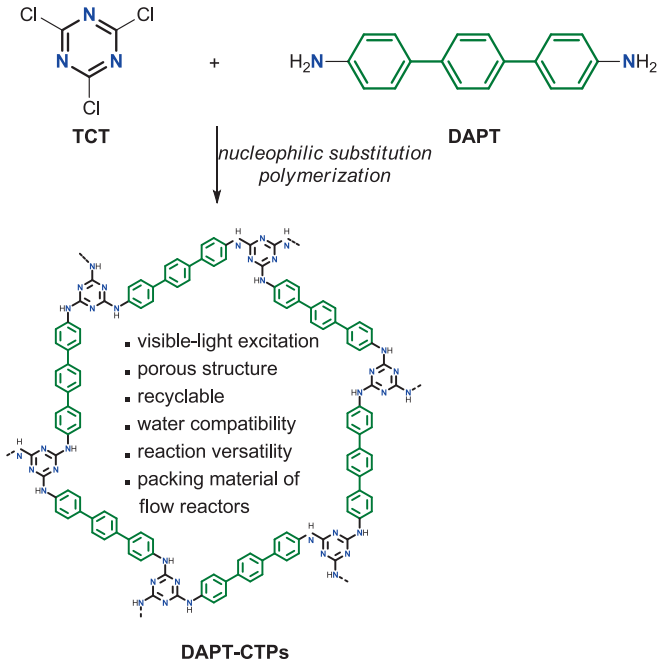

Fig. 1. Photocatalyst design, synthesis, and main features.

sulfide-to-sulfoxide aerobic oxidations [27,28] and cross-dehydrogenative couplings (CDCs) [29] of glycine precursors. The corresponding reaction mechanisms were duly examined by control experiments, indicating that metal-free **DAPT-CTPs** may effectively operate through electron transfer and energy transfer photoinduced pathways. **DAPT-CTPs** proved to be highly stable and recyclable materials operating under mild and sustainable conditions, utilizing air as the terminal oxidant and demonstrating compatibility with aqueous media. The robustness of **DAPT-CTPs** was utilized for the fabrication of fixed-bed photoreactors capable of functioning in prolonged experiments for the continuous-flow (CF) production of the active pharmaceutical ingredient (API) Ricobendazole. This work represents significant advances compared to previous studies by providing a complete photophysical characterization of the **DAPT-CTP** photocatalyst. Additionally, it demonstrates the synthetic versatility of this photocatalyst for producing added-value molecules, including APIs and non-proteinogenic α-amino acids (NPAAs) of biological relevance [30], in batch and flow setups.

2. Results and discussion

As anticipated, **DAPT-CTPs** were synthesized by nucleophilic substitution polymerization of equimolar **TCT** and **DAPT** using *N,N*-diisopropylethylamine (DIPEA) as the promoter (see the Supporting Information for details). By adapting a known procedure for the synthesis of triazine-based adsorbents [18,31], the semi-crystalline **DAPT-CTP$_{sc}$** was obtained in anhydrous dimethylacetamide (DMA) at 50-95 °C with a monomer concentration of 0.05 M, leading to a rapid but disordered 2D polymerization. The crystalline **DAPT-CTP$_{c}$** was prepared as described in a recent contribution on the application of CTPs in assembling lithium metal batteries [16]. Accordingly, equimolar **TCT** and **DAPT** were polymerized in anhydrous 1,4-dioxane at 90 °C under dilute conditions (0.002 M), which allowed for the formation of a regular 2D planar structure of the polymer. The powder X-ray diffraction (PXRD) of **DAPT-CTP$_{sc}$** and **DAPT-CTP$_{c}$** confirmed the mainly semi-crystalline and crystalline nature, respectively, of the as-prepared materials (Fig. 2a). **DAPT-CTP$_{c}$** exhibits sharper, stronger, and better-resolved diffraction reflections than **DAPT-CTP$_{sc}$**, indicating a higher degree of structural ordering and longer-range periodicity. The low-angle reflection at $2\theta \approx 5.2^{\circ}$ can be associated with an in-plane reflection of the ordered polymer. In contrast, **DAPT-CTP$_{sc}$** presents broader and less well-defined reflections, which align with its semi-crystalline nature. The superior degree of crystallinity for **DAPT-CTP$_{c}$** is also evidenced by an increase in peak intensity of a × 2 factor and paralleled by a slight simultaneous decrease in full-width-half-maximum (FWHM) of the main peak values, indicating the presence of a larger proportion of crystalline ordered polymer. This is also supported by a substantial reduction in the ratio between the broad background and the superimposed diffraction peak, from ca. 1:1 in **DAPT-CTP$_{sc}$** to ca. 1:4 in **DAPT-CTP$_{c}$**. The size of the crystalline domains is only slightly larger in **DAPT-CTP$_{c}$**, indicating that the main difference in the two materials is the amount of the amorphous phase rather than a qualitative difference in the size of the coherent domains that coexist within the amorphous phase. The average crystallite sizes (L) for the crystalline domains were indeed determined using the Debye Scherrer equation upon Gaussian fitting of the most intense $2\theta = 22.9^{\circ}$ peak, according to:

$$L = \frac{K\lambda}{\beta cos\acute{O}}$$

where K is the shape factor (typically 0.9), λ (1.54056 Å) is the wavelength of the X-ray used, β is the FWHM in radians of the XRD peak, and θ is the diffraction angle. The calculated crystallite sizes for **DAPT-CTP$_{c}$** and **DAPT-CTP$_{sc}$** were 11.5 and 10.2 nm, respectively.

The morphologies of **DAPT-CTP$_{sc}$** and **DAPT-CTP$_{c}$** were determined using scanning electron microscopy (SEM) (Fig. 2b,c). In detail, **DAPT-**

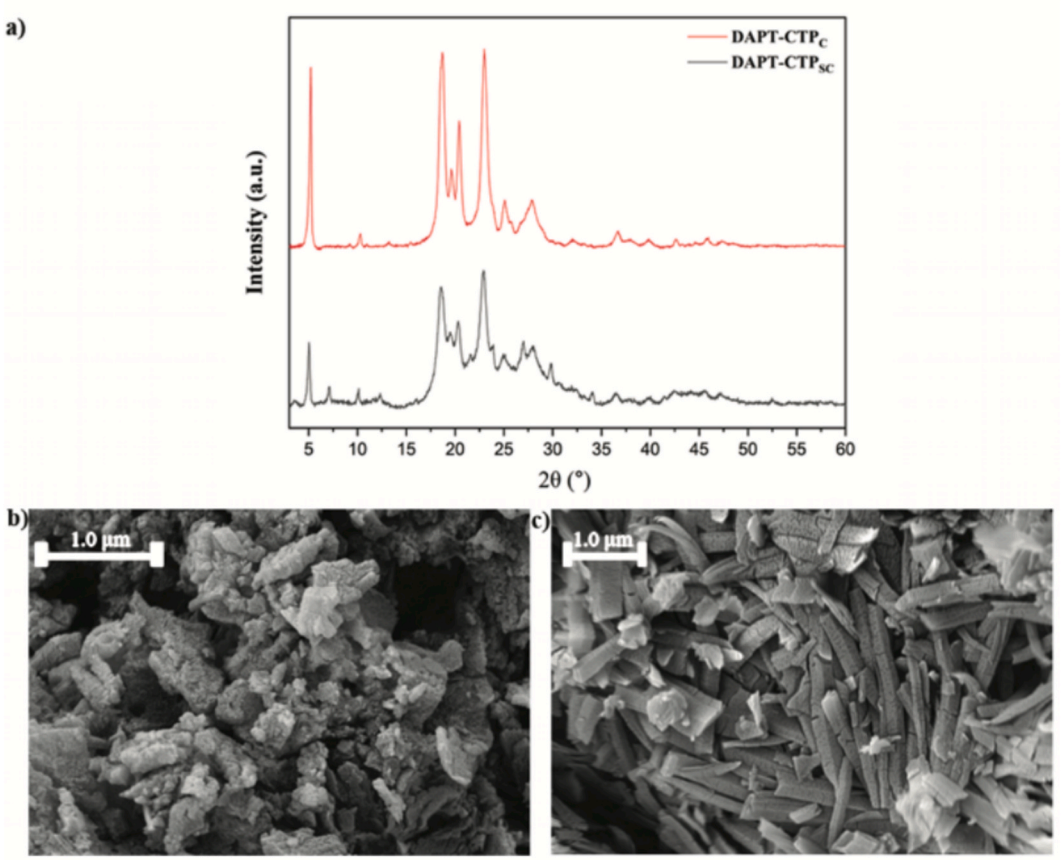

Fig. 2. Experimental PXRD patterns of **DAPT-CTP$_{sc}$** and **DAPT-CTP$_c$** (a). SEM images of **DAPT-CTP$_{sc}$** and **DAPT-CTP$_c$** (b,c).

CTP$_{sc}$ appeared as aggregated irregular lumps, while **DAPT-CTP$_c$** was characterized by micrometer-sized nanosheets, averaging 80–90 nm in thickness. Additionally, the uniform distribution of C and N atoms was verified from EDX- mapping analysis (Fig. S1, Supporting Information).

The nitrogen sorption measurements indicated that both polymers are mesoporous, as evidenced by their non-classical type IV adsorption–desorption isotherms, which exhibit hysteresis loops without a distinction condensation step at high relative pressure (Fig. 3). These hysteresis loops suggest the presence of slip-shaped mesopores or non-rigid aggregates of plate-like particles, consistent with the SEM observations. The Barrett-Joyner-Halenda (BJH) analysis shows similar average pore size of the semi-crystalline and crystalline polymers (~16 nm, Fig. S2). Likewise, Brunauer-Emmett-Teller (BET) surface area are comparable, with the values of approximately 16 m^2/g for **DAPT-CTP$_{sc}$** and 21 m^2/g for **DAPT-CTP$_c$**.

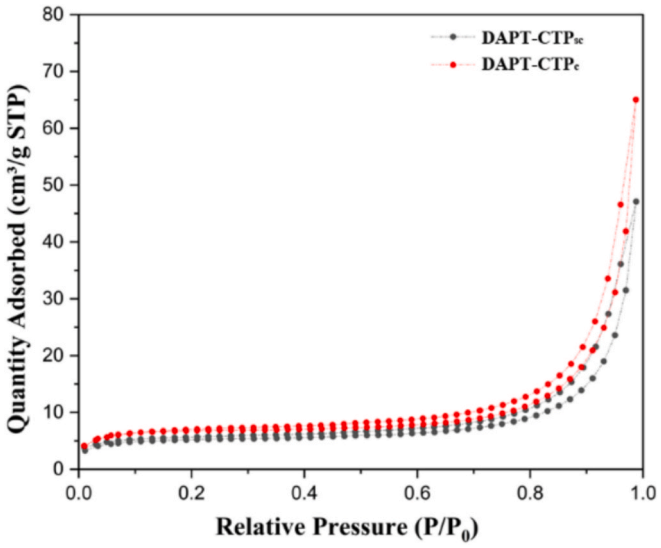

Fig. 3. Nitrogen adsorption–desorption isotherm of **DAPT-CTP$_{sc}$** (black line) and **DAPT-CTP$_c$** (red line). (For interpretation of the references to colour in this figure legend, the reader is referred to the web version of this article.)

The ATR-FTIR spectra of the synthesized triazine polymers confirmed the complete conversion of **DAPT** and **TCT** by the disappearance of the primary amine N–H stretch bands (3450–3180 cm^{-1}) and of the C-Cl peak (850 cm^{-1}), respectively (Fig. 4a). The occurrence of the iterative nucleophilic substitution was evidenced by the presence of the peak at 1230 cm^{-1} attributed to the stretching vibration of the exocyclic C-N bond. The regular 2D growth was also demonstrated by elemental analysis, observing C/N weight ratios in **DAPT-CTP$_{sc}$** (3.5) and **DAPT-CTP$_c$** (3.3) close to the theoretical value calculated for the polymer repeating unit (3.0; see the Supporting Information). The ^{13}C cross-polarization magic-angle-spinning (CP-MAS) solid-state NMR spectroscopy further confirmed the amine-linked terphenyl-based covalent triazine structure of **DAPT-CTPs** (Fig. 4b). In analogy with previous studies and soluble analogues [16,20], the peak at 165 ppm was attributed to the C signals of the triazine units, while the peaks at 136 and 127 ppm were assigned to the phenyl C signals of the terphenyl moieties. The thermogravimetric analysis (TGA) under air conditions of **DAPT-CTP$_{sc}$** and **DAPT-CTP$_c$** demonstrated comparable high thermal stability up to 350 °C (Fig. 4c).

The optical and photoelectrochemical properties of **DAPT-CTP$_{sc}$** and **DAPT-CTP$_c$** were next evaluated to assess the unknown potential of these materials in photocatalysis. From Fig. 5a, which presents the results of UV/Vis diffuse reflectance spectroscopy (DRS) experiments, it

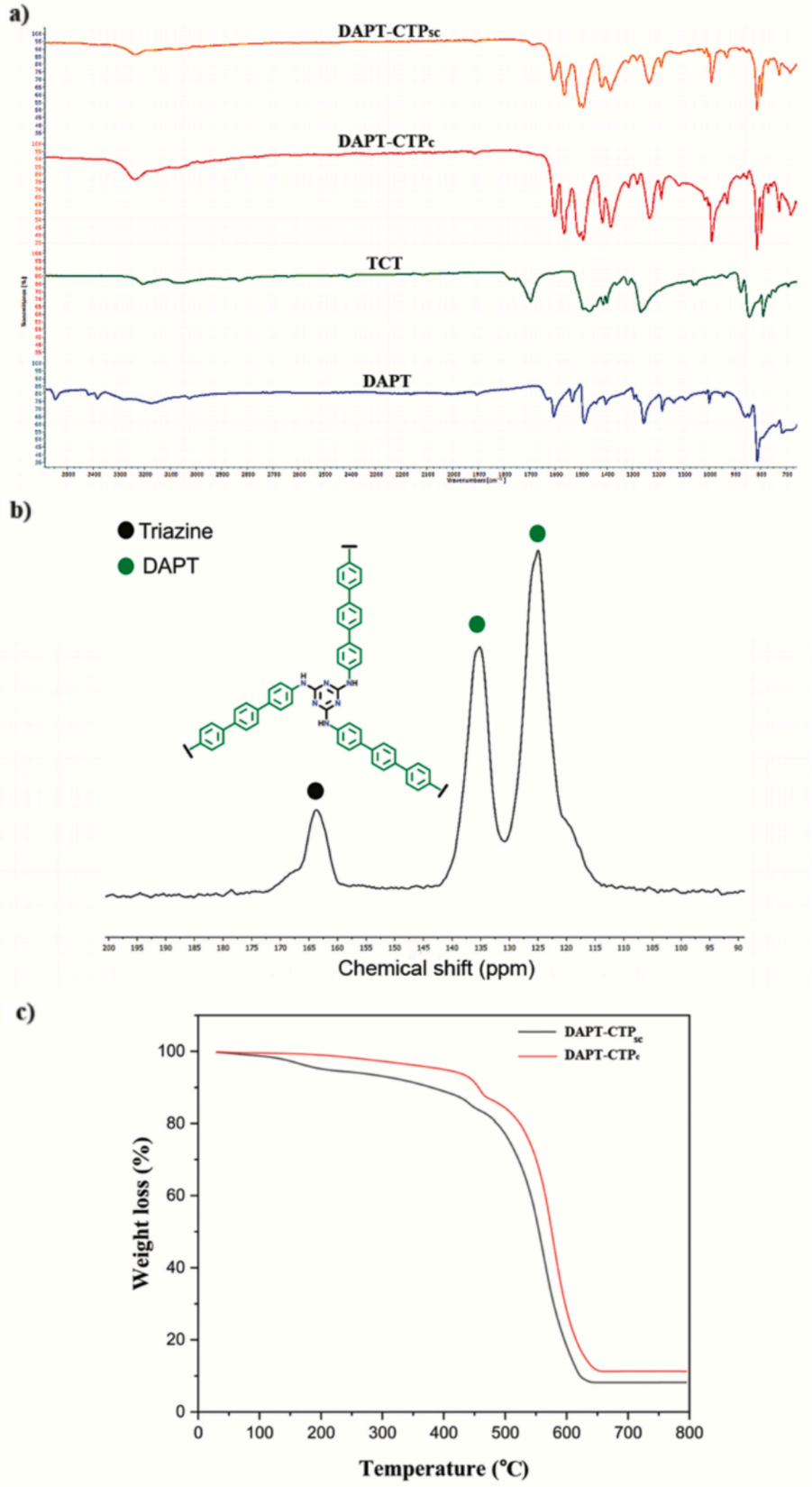

Fig. 4. ATR-FTIR spectra of **DAPT-CTP$_{sc}$** and **DAPT-CTP$_{c}$** in comparison with **TCT/DAPT** (a). ^{13}C CP-MAS NMR of **DAPT-CTP$_{sc}$** (b). Thermogravimetric curves of **DAPT-CTP$_{sc}$** and **DAPT-CTP$_{c}$** (c).

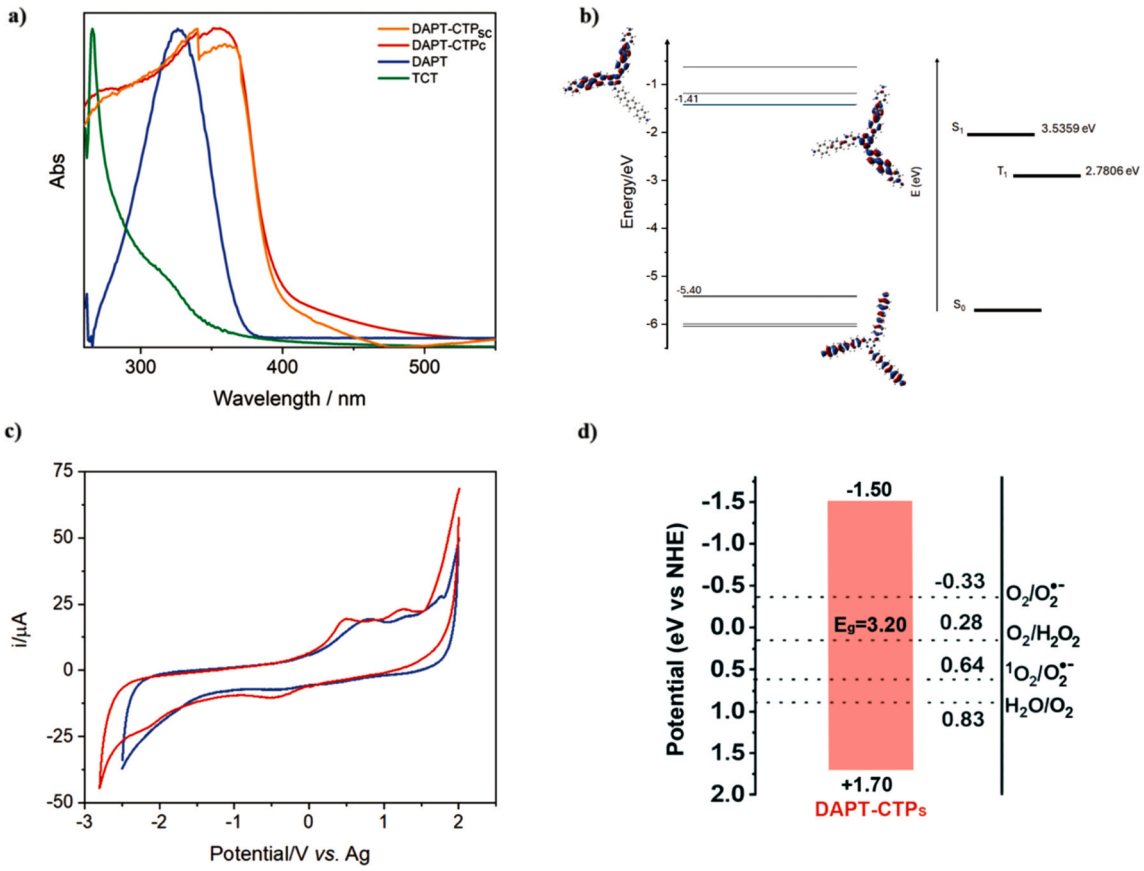

Fig. 5. UV/Vis DRS spectra of **DAPT-CTP$_{sc}$**, **DAPTP-CTP$_{c}$,** in comparison with **TCT**/ **DAPT** (a). Energy diagram showing the computed frontiers orbitals (left) and Jablonsky diagram for **DAPT-CTP** (right) (b). Cyclic voltammetry of **DAPT-CTP$_{sc}$** (red solid line) and **DAPTP-CTP$_{c}$** (blue solid line) dispersed in solution in CH_3CN/ $LiClO_4$ 0.1 M under N_2 atmosphere (c). Band structure diagram of **DAPT-CTPs** (d). (For interpretation of the references to colour in this figure legend, the reader is referred to the web version of this article.)

appears that **DAPT-CPTs** show a significantly broader spectral response compared to **DAPT**, extending into the edge of the visible region. Tauc plots (Fig. S3a,b) identify quite clearly an optical direct band gap of ca. 3.2 eV, regardless of the semi-crystalline or crystalline nature of this material. This value was confirmed from the crossing of the normalized emission and absorption spectra affording a zero-to-zero spectroscopic energy (E^{00}) of 3.19 eV (Fig. S4a), which is substantially lower than the 3.98 eV found for the model *p*-terphenyl (**PT**, Fig. S4b). The broad emission spectrum of **DAPT-CTPs** aligns with the radiative deactivation of singlet states (Fig. S5a-c). This behavior, influenced by the inherent heterogeneity of the polymeric solid, exhibits a multiexponential nature. This observation is consistent with a distribution of rate constants that arises from local micro- and nano-chemical environments, which affect, to varying degrees, the energy and the deactivation barrier of the lowest excited state. Deconvolution of the emission decay sampled at 425, 525 and 620 nm afforded an amplitude weighted lifetime confined in the sub-nanosecond region with values of 0.5, 0.7 and 0.65 ns, respectively. At all sampled wavelengths, the decay kinetics were satisfactorily modelled with a bi-exponential function, having a major component (at least 80%) with a lifetime in the interval 250–500 ps, and a smaller, longer-lived amplitude extending well in the ns timescale. The weight and lifetime of the long-lived component tend to increase when probing longer wavelengths. This explains the overall 15% increase in the averaged lifetime when moving from the emission maximum at 425 nm to longer wavelengths; this trend may be consistent with exciton trapping in shallow sub bandgap states. These effects are clearly absent in a simpler molecular entity like the model **PT**, for which a mono-exponential decay with $\tau \approx 1$ ns was found (Fig. S6).

TD-DFT calculations were used to rationalize the nature of the spectroscopic transitions in **DAPT-CTP** materials. First, the computational methodology was applied to the model **PT**, for which the absorption spectrum was well reproduced, with an error of 0.14 eV (Fig. S7). The experimental spectrum of **DAPT-CTP** was satisfactorily predicted by considering the optical transitions of fragments 1 and 2 (Figs. S8 and S9). In fragment 1, the triazine core bears three **DAPT** pendants each with free amine terminus, while in fragment 2 the free amino groups of **DAPT** are each attached to another triazine moiety. Our aim was to simulate the spectral properties of the bulk polymeric material using well-defined discrete molecular entities. This material is presumed to have all the amino groups of **DAPT** cross-linked with triazine. Additionally, we considered the potential presence of defects or surface states, where some amino groups of **DAPT** may remain unreacted. The spectral properties of fragments 1 and 2 are nearly identical both with regards to energy, orbital contributions, and relative intensity of their vertical transitions. Both in fragments 1 and 2, the lowest energy and strongest optical transition involve π-π* excitation from HOMO to a doubly degenerate LUMO, responsible for the main band centered at 3.5 eV, with an error in defect of just 0.07 eV compared to the experimental maximum (Fig. S10). Electron density difference maps (EDDMs) associated with the most intense transitions (Figs. S8 and S9) show that these incorporate some degree of charge transfer (CT) character as well. In fragment 1 bearing the free primary amine groups, we observe a shift in electron density from the free amine termini to the central triazine ring. A similar effect occurs in fragment 2; however, in this case, the peripheral triazine moieties also participate in electron delocalization. The hole density is predominantly found on the **DAPT** arms that bridge two triazine rings. Plotting the vertical transitions with an arbitrary FWHM of 3000 cm^{-1} reproduces the overall shape of the experimental spectrum

of the solid **DAPT-CTP$_{sc}$** reasonably well. The same TD-DFT methodology was used also to predict, in terms of vertical energy, the positioning of the lowest triplet state, which was found ca. 0.7 eV lower than the first singlet state, at ca. 2.8 eV above the ground state (Fig. 5b). Such triplet energy guarantees ample driving force to promote energy transfer to triplet oxygen to generate both reactive $^1\Delta$ and $^1\Sigma$ states of O_2 [32]. Clear evidence of triplet population via intersystem crossing, following the spin-allowed optical excitation of **DAPT-CTP$_{sc}$**, is gained by transient absorption spectroscopy (TAS). This analysis showed, upon 355 nm excitation, the formation, within the instrument response function (IRF) of our spectrometric apparatus, of a long-lived excited state, whose general features are reminiscent of what is found for the simpler model **PT** (Fig. S11). The T_1 state of **DAPT-CTP$_{sc}$** exhibits a broad fingerprint due to $T_1 \rightarrow T_n$ transitions that cover the entire visible range (Fig. S12). This state survives, following a multiexponential decay kinetics, for hundreds of microseconds under deareated conditions (N_2 purging). However, consistent with our assignment, it is quenched approximately within the IRF upon exposure to oxygen (air). This indicates highly efficient energy transfer ($\approx 1.4 \times 10^7$ s^{-1}) to the $^3\Sigma$ state of molecular oxygen and the consequent generation of singlet oxygen ($^1O_2$). It is interesting to observe that, within the sensitivity of TAS, no meaningful residual absorption is detected in the presence of oxygen. This observation suggests a minor optical contribution from long-lived charge-separated states (electron/hole pairs), which result from the separation of the excitonic states initially created within the solid.

The Hirschfeld analysis of the atom contribution to the frontier orbitals points out a significant amplitude (from 4 to 6%) of the free amino group in fragment 1 in the HOMO (Fig. S13; Table S1). Such a contribution is substantially reduced at the LUMO (ca. 1%; Table S2), indicating a degree of charge transfer that may contribute to improving the light harvesting efficiency and spectral sensitivity via an increased transition dipole moment. A smaller contribution by nitrogen (ca. 3.5%) is observed also on the triazine-terminated fragment 2, coming, at the HOMO level, mostly from the bridging NH groups connecting the triazine to the *p*-terphenyl chain (Fig. S14; Table S3). At the LUMO level (Table S4), major contributions come from aromatic carbon atoms of the *p*-terphenyl units, showing also in this case some degree of charge transfer character, beneficial for the optical properties of the material for the same reasons explained above.

Next, we attempted to address the redox properties of these materials. Although a rigorous electrochemical analysis of these species was limited by the substantial irreversibility of the redox processes, we were able to obtain a broad picture of the density of occupied and empty states in these materials. The cyclic voltammetry (CV) analysis revealed two main unresolved processes extending between +1.5/2 V and −1.5/−2 V *vs* Ag/Ag$^+$, respectively, for both **DAPT-CTP$_{sc}$** and **DAPT-CTP$_c$** dispersed in solution (Fig. 5c). Notably, CV supported our hypothesis regarding the favorable interaction between **DAPT-CTPs** and oxygen, which leads to the efficient quenching of the triplet state. In fact, an enhanced reduction process was observed in the presence of oxygen by **DAPT-CTP** films supported on both graphite and fluorine-doped tin oxide (FTO) ohmic collectors (Fig. S15). To investigate deeper the nature of **DAPT-CTP**-oxygen interaction, the electrostatic potential (ESP) maps of these polymers were generated based on the optimized molecular fragments 1 and 2. The ESP maps show that the terminal NH_2 and NH bridging amino groups are centers of positive electrostatic potentials, thereby confirming the p-π conjugated structure of the materials. In particular, the free amino pendants present the higher positive potentials (fragment 1, Fig. S16). The bulk of the polymers, simulated by the triazine-terminated fragment 2, also presents positive regions, especially near the triazine groups that are linked to the *p*-terphenyl units (Fig. S17). In contrast, the *p*-terphenyl moieties represent areas of increased negative potential with higher electron density, suggesting their involvement in nucleophilic interactions with molecular oxygen.

Summarizing the key aspects of utilizing **DAPT-CTPs** as photocatalysts, DFT calculations revealed a vertical energy of 3.5 eV that, considering the vibrational broadening results, is in a good match with UV/Vis DRS and individuate an onset of photoabsorption at the edge of the visible region. As shown in Fig. 5a, the absorption band edge was detected in the visible-light region at $\lambda_{max} \approx$ 380–390 nm for both **DAPT-CTP$_{sc}$** and **DAPT-CTP$_c$**, corresponding to optical band gaps around 3.2 eV. The experimental positioning of acceptor states determined for **DAPT-CTPs** by cyclic voltammetry measurements (ca. −1.5 eV *vs.* NHE) was consistent with the calculated value (Fig. 5c and Supporting Information). By combining the onset of the reductive processes with the optical band gap, the edge position of the occupied states was estimated at ca. +1.7 eV *vs.* NHE (Fig. 5d). Compared with previously synthesized triazine polymers based on furan, thiophene [33] or *p*-terphenyl [20,34] moieties in place of **DAPT** as the spacer of triazine units, **DAPT-CTPs** exhibit appreciably more negative values of the empty states (−1.5 eV *vs.* −1.4/-0.7 eV). This trend aligns with the discrete molecule **DAPT** that displays both π-π and p-π conjugation structures [35], thereby opening avenues for the effective application of **DAPT-CTPs** in ROS generation ($E_{red}(O_2/O_2\bullet-) = -0.33$ eV *vs.* NHE; $E_{red}(^1O_2/O_2\bullet-) = +0.64$ eV *vs.* NHE).

The direct evidence for ROS generation was obtained from electron spin resonance (ESR) experiments, using 5,5-dimethyl-1-pyrrole-*N*-oxide (DMPO) and 2,2,6,6-tetra-methyl-1-piperidine (TEMP) as the trapping agents for $O_2\bullet-$ and $^1O_2$, respectively. Measurements were conducted in both EtOH and aqueous EtOH solutions to evaluate potential variations in the photooxidations performed in an aqueous medium (see below). Accordingly, the suspensions of DMPO and **DAPT-CTP$_{sc}$** in EtOH or EtOH-H_2O 1:1 mixture were transferred into a flat quartz cell and directly irradiated (Hg medium pressure lamp with a cut-off filter, $\lambda \geq 400$ nm) in the ESR cavity. No signals were detected in the dark (Fig. 6a, black line) or in the absence of photocatalyst. Upon photoexcitation of an aerated suspension of **DAPT-CTP$_{sc}$** in EtOH containing DMPO, a triplet of doublets was formed, exhibiting hyperfine splitting constants (hfsc) of $a_N = 13.7$ G and $a_H = 9.0$ G (red line). The observed pattern and hfsc values can be attributed to the paramagnetic adduct [DMPO-OOH]•, which arises from the formation of $O_2\bullet-$ [36]. When the trapping experiment was conducted in a 1:1 mixture of EtOH-H_2O, a very weak signal was obtained (blue line), likely due to multiple overlapping signals. A comparison of the red and blue lines indicates the presence of both [DMPO-OOH]• and [DMPO-OH]• adducts. The latter is derived from the hydroxyl radical •OH and displays four lines in a 1:2:2:1 ratio, with $a_N = a_H = 14.4$ G (signals marked). The overlapping spectrum aligns with that reported by Makino and co-workers [36], where the overlapping signals of the two adducts are simulated in varying ratios. Additionally, Fig. 6b shows that the photoexcitation of an aerated suspension of **DAPT-CTP$_{sc}$** in EtOH or in EtOH-H_2O 1:1 mixture containing TEMP leads to the formation of a triplet, which can be attributed to the formation of the stable radical 2,2,6,6-tetramethyl-1-piperidinyloxy (TEMPO) [37]. This result indicates that $^1O_2$ is formed as well, in agreement with the TAS finding.

Sulfoxides represent a highly valuable class of organic compounds that are extensively utilized in the pharmaceutical [38,39], agrochemical [40], and polymer industries [41]. Among various synthetic methods, the selective aerobic oxidation of sulfides via visible-light photocatalysis has emerged as the preferred strategy for producing sulfoxides under mild and environmentally friendly conditions [42]. This development has spurred significant research into the production of low-cost, metal-free heterogeneous photocatalysts, which may function as molecular reactors in the presence of aerobic oxygen to form the reactive superoxide radical anion ($O_2\bullet-$; electron transfer mechanism) and/or singlet oxygen ($^1O_2$; energy transfer mechanism) [43]. Hence, given their potential to interact with oxygen on the surface [19,20] and generate ROS (Fig. 5d), the synthesized **DAPT-CTPs** were evaluated in the model aerobic oxidation of thioanisole **1a** (Table 1). At the outset of the study, the reaction parameters were optimized with the semi-crystalline **DAPT-CTP$_{sc}$** (20 mol%) due to its easier availability using EtOH as the preferred green solvent. The phenomenon of sulfide self-

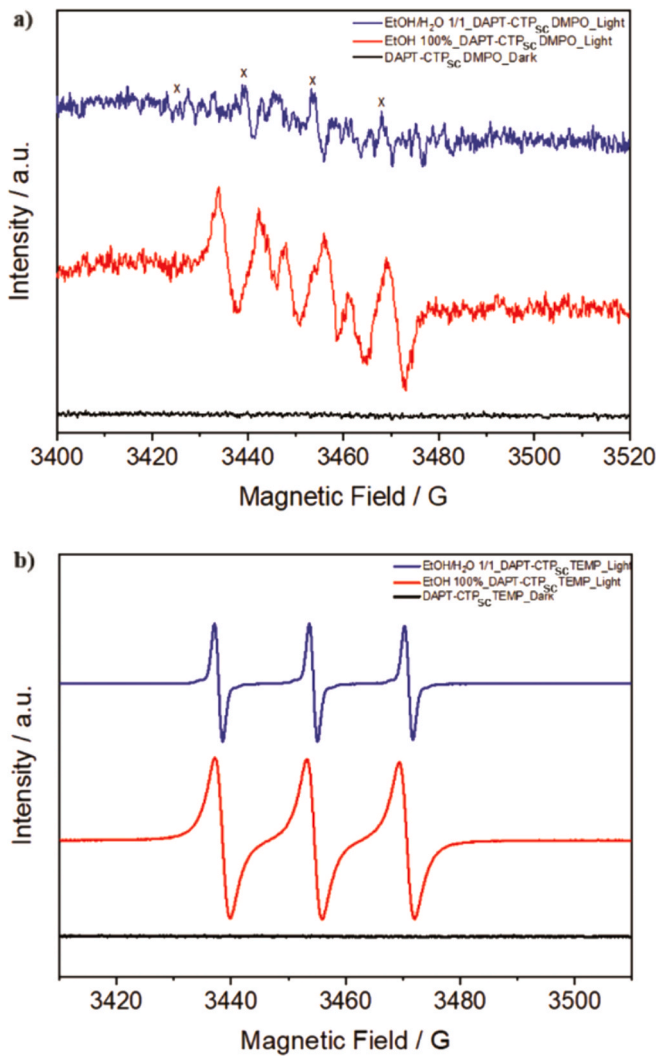

Fig. 6. ESR spin trapping spectra obtained upon photoexcitation ($\lambda \geq 400$ nm) of **DAPT-CTP$_{sc}$** suspended in EtOH 100% (red line) or EtOH-H_2O 1:1 mixture (blue line) containing the spin trap DMPO (5×10^{-2} M) (a) and TEMP (1×10^{-2} M) (b). Dark conditions before irradiation (black line). (For interpretation of the references to colour in this figure legend, the reader is referred to the web version of this article.)

excitation without the need for an external photocatalyst when exposed to specific wavelengths is a recognized process, which can generate singlet oxygen and activate electron transfer events [28,44]. Hence, we initially verified that irradiating the reaction mixture with a purple Kessil lamp (power density: 200 mW/cm^2) for 3 h at 390 nm led to the complete conversion of **1a** (0.2 M) in the absence of the photocatalyst with modest sulfoxide **2a**/sulfone **3a** selectivity (entry 1). After some experiments with different light sources and filters, we found that utilization of a mercury-xenon lamp in combination with a long-pass filter at 400 nm (power density: 250 mW/cm^2) afforded the target phenyl methyl sulfoxide **2a** with complete selectivity in 85% yield after 16 h of irradiation without any contribution of the noncatalytic background oxidation (entries 2–3; Fig. S18). It has been reported that sulfide oxidation can occur in water media through a mechanism induced by hydroxyl radical (•OH), a process that is significantly amplified when molecular oxygen is present [45]. Accordingly, the model aerobic sulfoxidation was tested in a 1:1 EtOH:H_2O mixture, leading to the quantitative formation of **2a** within the same reaction time (entry 4). Control experiments demonstrated that both air and light are crucial to promote the process (entries 5–6). Additionally, it was found that halving the

Table 1
Optimization of aerobic sulfoxidation.[a]

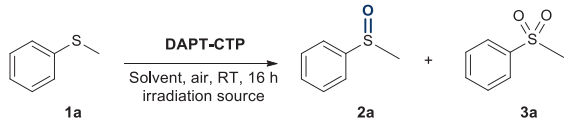

Entry	DAPT-CTP	Lamp (nm)	Solvent	**2a** (%)[b]	**3a** (%)[b]
1	–	390[c]	EtOH	62	38
2	–	>400[d]	EtOH	–	–
3	**DAPT-CTP$_{sc}$**	>400[d]	EtOH	85	–
4	**DAPT-CTP$_{sc}$**	>400[d]	EtOH:H_2O[e]	>95	–
5[f]	**DAPT-CTP$_{sc}$**	>400[d]	EtOH:H_2O[e]	–	–
6	**DAPT-CTP$_{sc}$**	no light	EtOH:H_2O[e]	–	–
7[g]	**DAPT-CTP$_{sc}$**[g]	>400[d]	EtOH:H_2O[e]	61	–
8[h]	**DAPT-CTP$_{sc}$**	>400[d]	EtOH:H_2O[e]	54	–
9	**DAPT-CTP$_{sc}$**	427[i]	EtOH:H_2O[e]	86	–
10	**DAPT-CTP$_{c}$**	>400[d]	EtOH:H_2O[e]	>95	–
11[h]	**DAPT-CTP$_{c}$**	>400[d]	EtOH:H_2O[e]	51	–

[a] **1a** (0.2 mmol), **DAPT-CTP** (20 mol%), solvent (1 mL), irradiation for 16 h under air atmosphere (balloon). See the Supporting Information for details. [b] Detected by ^{1}H NMR of the crude reaction mixture with ethylene carbonate as internal standard. [c] Purple Kessil lamp. [d] Hg-Xe lamp. [e] 1:1 mixture. [f] Reaction performed under argon. [g] **DAPT-CTP$_{sc}$**: 10 mol%. [h] Reaction time: 6 h. [i] Blue Kessil lamp.

amount of **DAPT-CTP$_{sc}$** or reducing the reaction time resulted in a significant decrease of the process efficiency (entries 7–8). An appreciable reduction in the yield of **2a** (86%) was observed when the reaction mixture was irradiated with the LED light at 427 nm (blue Kessil lamp; power density: 210 mW/cm^2; entry 9). Finally, utilization of crystalline **DAPT-CTP$_{c}$** (20 mol%) in place of the semi-crystalline analogue did not lead to any improvement in the reaction outcome (entries 10–11). This result suggests that the increased structural order of **DAPT-CTP$_{c}$** has less influence compared with other properties, such as surface area and redox potentials, which are comparable for both materials.

The substrate scope of sulfides **1** was then examined under the optimized conditions of Table 1, entry 4. Authentic samples of sulfones **3** were prepared by standard methods to carefully evaluate the reaction selectivity, and the composition of the EtOH-H_2O mixture was suitably adjusted to obtain a homogeneous solution of reactants (Supporting Information). All tested sulfides **1** were converted into the corresponding sulfoxides **2**, achieving complete selectivity and moderate to excellent isolated yields (Table 2; see Table S8 for a comparison of catalyst performance with other CTPs). The thioanisole derivatives bearing electron-withdrawing halogen groups and the electron-donating methoxy group in *para*- or *meta*-positions afforded the corresponding sulfoxides **2b-f** with high efficiency (91–88%), while the *ortho*-substituted analogues **2g** and **2h** were obtained in poorer yields (77% and 55%) despite the increased reaction time (24 h). Gratifyingly, the disclosed methodology was also compatible with an aldehyde aryl substituent (**2i**, 90%) as well as allyl, benzyl, and dialkyl sulfides (**2j**, 70%; **2k**, 72%; **2l**, 67%; **2m**, 64%).

The use of CTPs to facilitate divergent chemical transformations in a controllable fashion guided by similar mechanistic rationales is highly desirable, but it is quite rare in the literature, particularly in the case of valuable C–C forming reactions [7,9]. Therefore, research on the synthetic potential of the newly developed **DAPT-CTPs** was extended to the photocatalytic cross-dehydrogenative coupling (CDC) between glycine and indole derivatives to access pharmaceutically relevant NPAAs [46]. This two-step process is unprecedented with CTP photocatalysts and involves the initial aerobic oxidation of the amino acid substrate, which is promoted by photogenerated ROS [47]. This oxidation results in the formation of an imine or iminium intermediate, which is subsequently intercepted by the carbon nucleophile in a Friedel-Crafts (FC) alkylation reaction (*vide infra* for mechanistic details). Our group contributed to

Table 2
Substrate scope.[a]

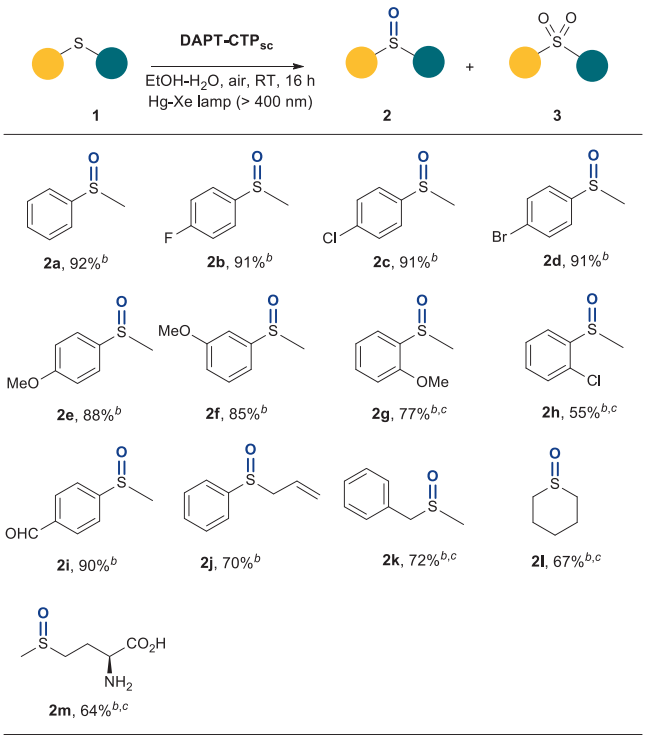

[a]**1** (0.2 mmol), **DAPT-CTP$_{sc}$** (20 mol%), EtOH-H_2O (1 mL), irradiation (Hg-Xe lamp, $\lambda > 400$ nm) for 16 h under air atmosphere (balloon). See the Supporting Information for details. [b]Isolated yield. [c]Reaction time: 24 h.

this area of research by reporting on an effective photoredox CDC protocol mediated by mesoporous graphitic carbon nitride [24]. Based on that study, the model coupling of ethyl 2-(phenylamino)acetate **4a** (1.3 equiv.) and indole **5a** (0.1 M) was investigated in EtOAc with **DAPT-CTP$_{sc}$** (20 mol%) as the photocatalyst, while carefully verifying the distribution of the reaction by-products. These are the imine **7** generated by overoxidation of the target product **6aa** and the bis-adduct **8** derived from the photo-assisted C-N cleavage of **6aa** followed by the second

Table 3
Optimization of aerobic cross-dehydrogenative coupling.[a]

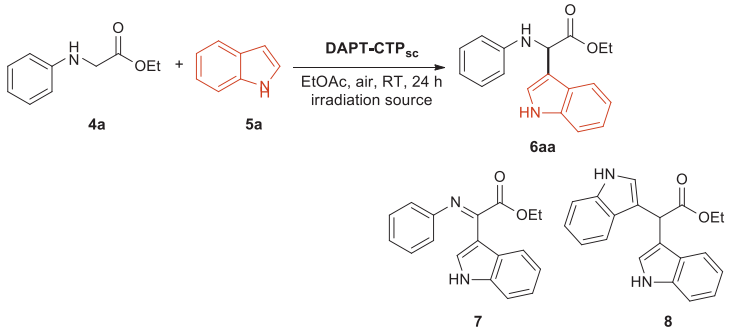

Entry	Lamp (nm)	Conversion (%)	**6aa** (%)[b]	**7** (%)[b]	**8** (%)[b]
1[c]	390[d]	53	31	7	5
2[c]	>400[e]	37	25	5	7
3[c]	>420[e]	–	–	–	–
4[f]	>420[e]	73	62	5	6
5	>420[e]	85	74	<5	6
6[g]	>420[e]	–	–	–	–
7	no light	–	–	–	
8	427[h]	82	71	<5	8

[a]**4a** (0.13 mmol), **5a** (0.1 mmol), **DAPT-CTP$_{sc}$** (20 mol%), EtOAc (1 mL), irradiation for 24 h under air atmosphere (balloon). See the Supporting Information for details. [b]Detected by ^{1}H NMR of the crude reaction mixture with durene as internal standard. [c]Absence of photocatalyst. [d]Purple Kessil lamp. [e]Hg-Xe lamp. [f]**DAPT-CTP$_{sc}$** (10 mol%). [g]Reaction performed under argon. [h]Blue Kessil lamp.

addition of **5a** (Table 3). Irradiation of the reaction mixture without the photocatalyst at the maximum absorption wavelength of **DAPT-CTP$_{sc}$** (390 nm, purple Kessil lamp) initiated the background oxidation process, leading to the formation of a significant amount of product **6aa** (31%; entry 1). After some experimentation, it was determined that this undesired pathway was inhibited by using a mercury-xenon lamp fitted with a long-pass filter at 420 nm (power density: 220 mW/cm^2; entries 2–3). The **4a/5a** CDC was promptly optimized using **DAPT-CTP$_{sc}$** (entries 4–5), while also confirming that the disclosed process does not occur in the dark or in the absence of air (entries 6–7). Finally, it was observed that the exposure of the reaction mixture to the LED light at 427 nm (blue Kessil lamp) has minimal impact on the process efficiency (entry 8).

The generality of the photoinduced CDC was successfully demonstrated by the combination of *N*-aryl glycines **4** and indoles **5** displaying different steric and electronic features (Table 4). Satisfactory yields were detected in the formation of amino esters **6aa-6fa** (74–62%) starting from the corresponding glycines **4** bearing electron-withdrawing and electro-donating groups in *para*- and *ortho*-positions of the phenyl ring. The variation of indole **5** showed that electron-poor substrates (**6ab**, 80%; **6ac**, 72%) exhibit better reactivity compared to their electron-rich counterparts (**6ad**, 55%; **6ae**, 51%). This result is explained by the higher acidity of the proton in the C3 position of the indole ring, which facilitates the rearomatization step in the FC reaction. Satisfyingly, the methodology also exhibited compatibility with *N*-substituted indoles (**6af**, 65%; **6ag**, 74%).

The recyclability of **DAPT-CTP$_{sc}$** was finally examined in the **4a/5a** coupling to demonstrate its robustness under operational conditions. Over five runs, no loss of activity was noted for the heterogeneous photocatalyst, which was simply filtered, washed with ethyl acetate, and dried between experiments (Fig. 7). The FT-IR spectrum of **DAPT-CTP$_{sc}$** after the recycling experiment showed minimal changes compared to that of the fresh material (Fig. S19), confirming the excellent stability of **DAPT-CTPs** in aerobic oxidation processes.

At this stage of the study, quenching experiments were conducted to clarify the role of each reactive oxygen species in the reaction mechanism of the two aerobic oxidation processes. In the sulfide-to-sulfoxide oxidation (Scheme 1a), the addition to the reaction system of *p*-benzoquinone (BQ), a scavenger of $O_2\bullet-$, completely inhibited the process (**2a** < 5%), indicating the participation of the superoxide radical anion in the process. The introduction of sodium azide (NaN_3), a quencher of $^1O_2$, led to a significant reduction of the reaction yield (20%). Similarly, when KI was used as a hole (h^+) scavenger, only 8% of **2a** was produced. Furthermore, the addition to the aqueous reaction mixture of triethylamine (TEA), a scavenger of hydroxyl radical (•OH), decreased the reaction yield to 18%. Control experiments were also carried out in the

Table 4
Substrate scope.[a]

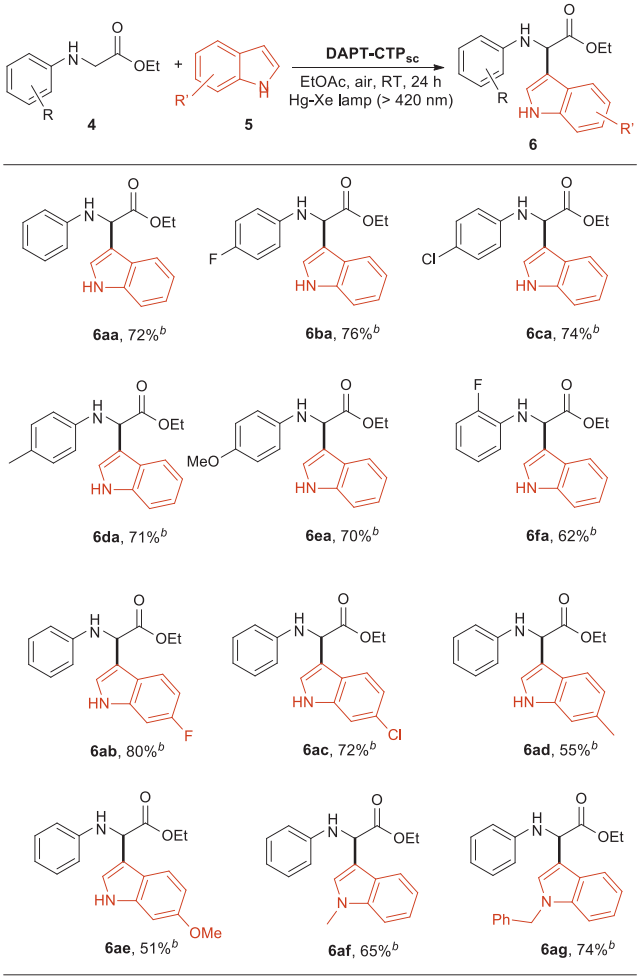

[a]**4** (0.13 mmol), **5** (0.1 mmol), **DAPT-CTP$_{sc}$** (20 mol%), EtOAc (1 mL), irradiation for 24 h under air atmosphere (balloon). See the Supporting Information for details.
[b]Isolated yield.

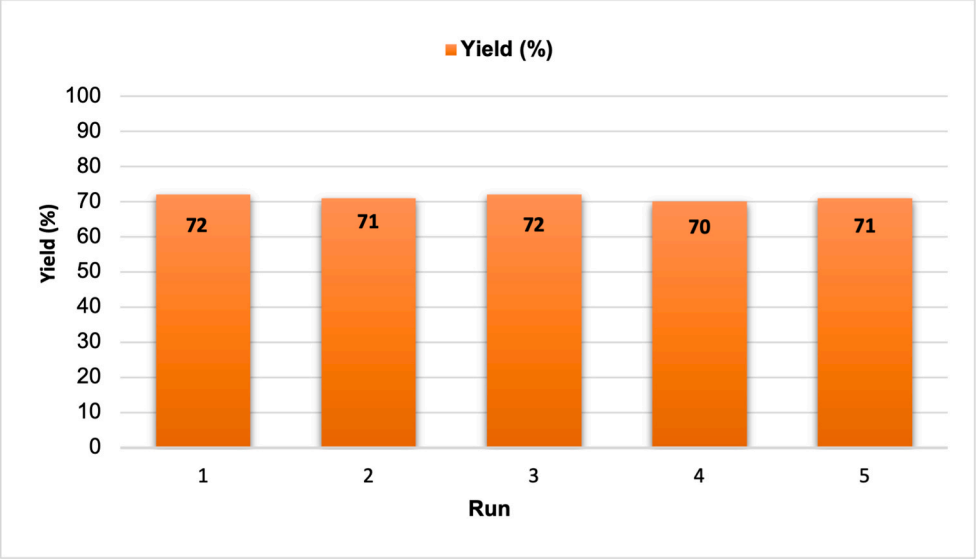

Fig. 7. Recycling experiments (**4a/5a** coupling).

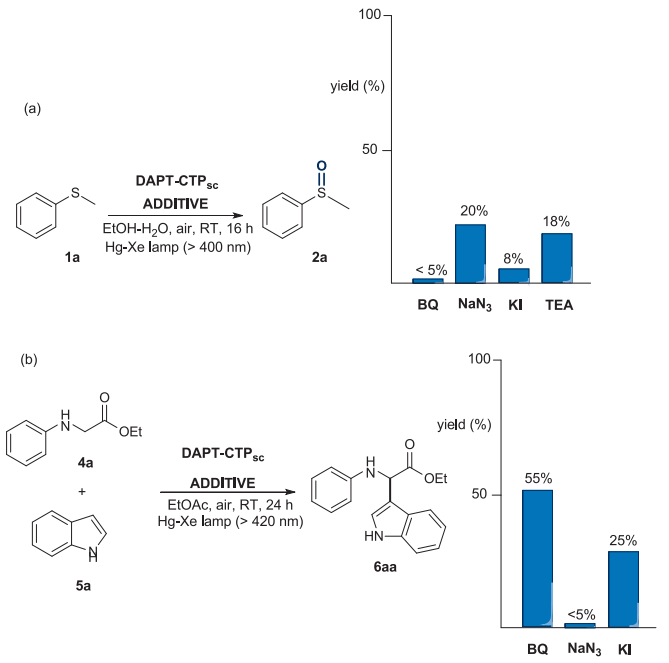

Scheme 1. Quenching experiments of the model sulfide-to-sulfoxide oxidation (a) and cross-dehydrogenative coupling (b).

model CDC (Scheme 1b), highlighting the essential roles of superoxide (O_2•−), holes (h^+), and singlet oxygen ($^1O_2$) in the photooxidation step of the **4a**/**5a** coupling.

Based on the results presented above and earlier studies [28,43–48], the mechanistic hypotheses outlined in Schemes 2 and 3 can be proposed for the aerobic photo-oxygenations promoted by **DAPT-CTP**. First, the visible-light irradiation of the photocatalyst initiates the excitation of electrons from the occupied to the acceptor states. Then, the activation of O_2 into O_2•− and $^1O_2$ occurs through singlet electron transfer (SET) and energy transfer (ET) processes, respectively, the latter involving relaxation to the triplet state via intersystem crossing (ISC). In the sulfide-to-sulfoxide conversion (Scheme 2), the photo-generated holes can oxidize the electron-rich thioanisole **1a** to the radical cation **I**, which in turn is intercepted by O_2•− to generate the persulfoxide **II** [49]. This intermediate reacts with a second molecule of **1a** through nucleophilic addition to form the unstable hypervalent species **III**, which finally degrades into two molecules of sulfoxide **2a** [50]. Alternatively, $^1O_2$ can attack **1a** to produce the diradical **IV**, which coexists with the zwitterionic intermediate **II** and reacts with a second molecule of **1a** to form **III** and then sulfoxide **2a**. [49,51]. However, based on the results of our photoelectrochemical study on **DAPT-CTP**, the possibility of direct formation of O_2•− and the radical cation **I** from **1a** and $^1O_2$ via SET cannot be excluded (dotted box). Additionally, the target sulfoxide **2a** can also be obtained through the addition of the photogenerated hydroxyl radical to **1a** [52]. This process generates the radical intermediate **V**, which subsequently intercepts a second •OH, leading to **2a** via the elimination of water [48].

In the photocatalytic CDC reaction (Scheme 3), drawing from our and other group studies [24,53,54], it is supposed that aryl glycine **4a** is oxidized by the photogenerated holes to form the radical cation **VI**, which undergoes fast deprotonation leading to the carbon-centered radical **VII**. This species recombines with O_2•− to generate the peroxidic intermediate **VIII** that releases the hydroxyl peroxide anion (HOO–) and the imine **IX**, ultimately participating in the Friedel-Crafts reaction with indole **5a**. Moreover, previous observations [55] suggest a mechanism via two-hydrogen atom abstraction (HAA), where $^1O_2$ may abstract hydrogen atoms from the N–H and the C–H in α position of **4a** to produce H_2O_2 and the imine **IX** [55].

The process intensification of the disclosed methodology was evaluated addressing the continuous-flow synthesis of **Ricobendazole**, a drug employed in the treatment of gastrointestinal infections [56] and a potential anticancer agent [57]. For this purpose, taking advantage of our previous experience in the field of photocatalytic CF processes [25,58], a reactor named **R$_1$-DAPT-CTP$_{sc}$** was assembled by feeding a glassy column with **DAPT-CTP$_{sc}$** (300 mg) and glassy beads (4.9 g, 425–600 μm diameter). By means of an HPLC pump, a solution of sulfide **Albendazole** in DMSO was delivered to a Y-mixer (Fig. 8), where it was mixed with a continuous-flow of air, controlled through a mass flow controller (MFC). DMSO was chosen as the preferred reaction solvent due to the known solubility issues of both **Albendazole** and **Ricobendazole** in hydroalcoholic solutions, following verification of its inertness under the photocatalytic CF conditions. The resulting air–liquid segmented flow was connected to the photoreactor (Fig. S20), which was irradiated by a Hg-Xe lamp equipped with a long-pass filter at 400 nm (Fig. 8, Setup A). Notably, working under a segmented flow regime is necessary to provide the right amount of oxygen into the

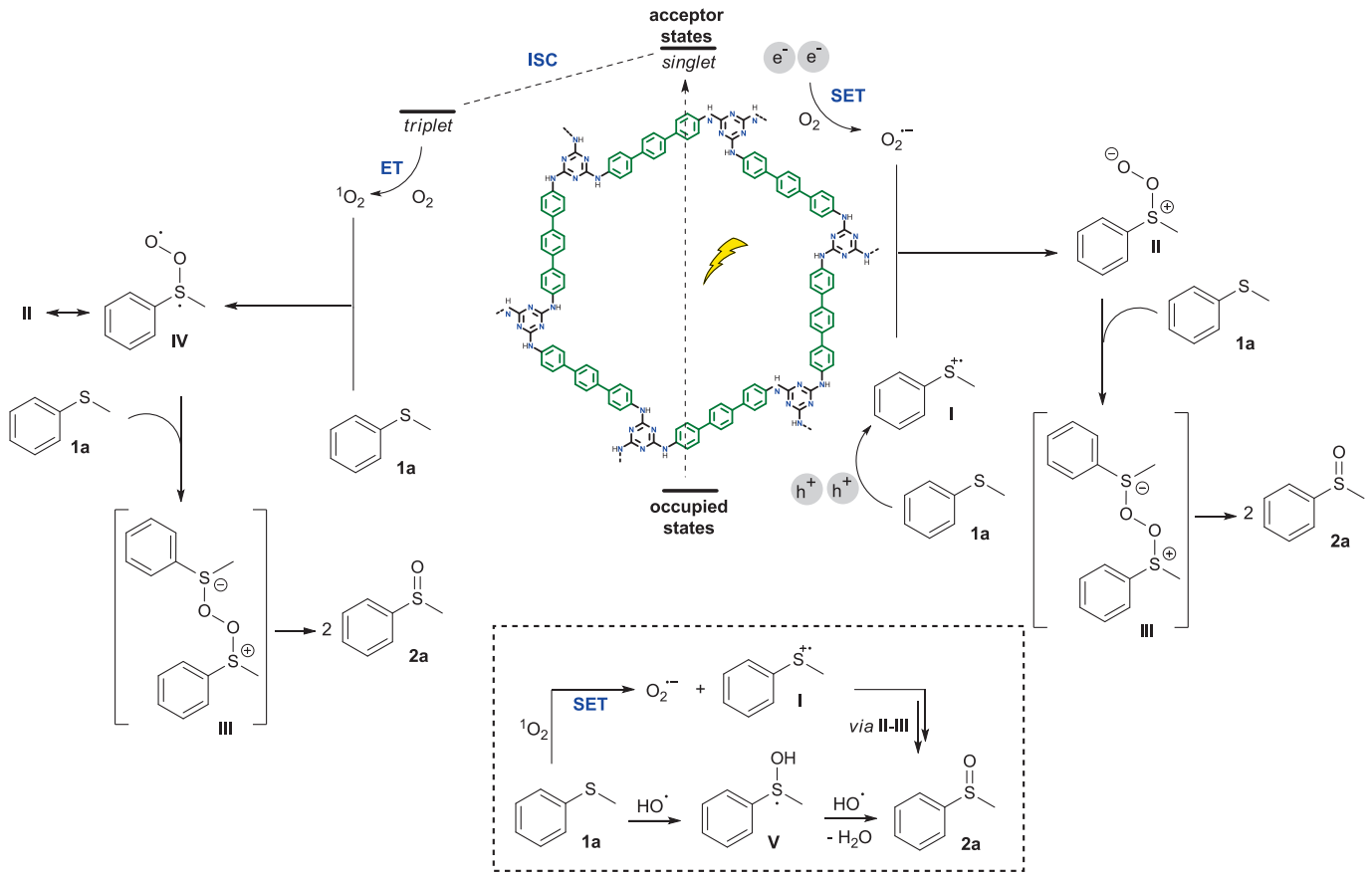

Scheme 2. Proposed reaction mechanisms for the photocatalytic aerobic sulfoxidation promoted by **DAPT-CTP**.

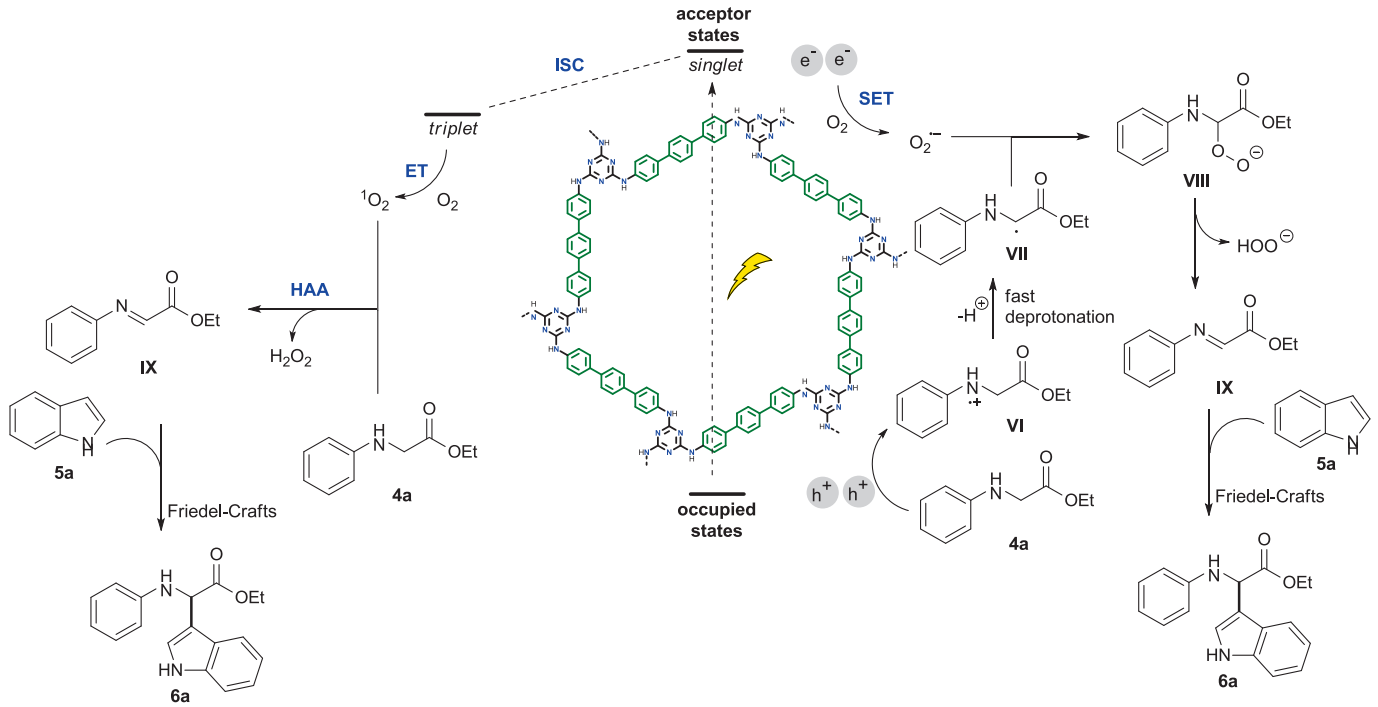

Scheme 3. Proposed reaction mechanisms for the photocatalytic aerobic cross-dehydrogenative coupling promoted by **DAPT-CTP**.

solution; indeed, the use of an aerated solution of **Albendazole** without using a MFC resulted in the quantitative recovery of the starting sulfide. After a preliminary optimization of the process parameters, working by flowing 5 μL/min of **Albendazole** solution (0.05 M in DMSO) and 50 μL/min of air allowed the achievement of the steady state after 120 min, with a satisfactory 88% yield of **Ricobendazole** and negligible

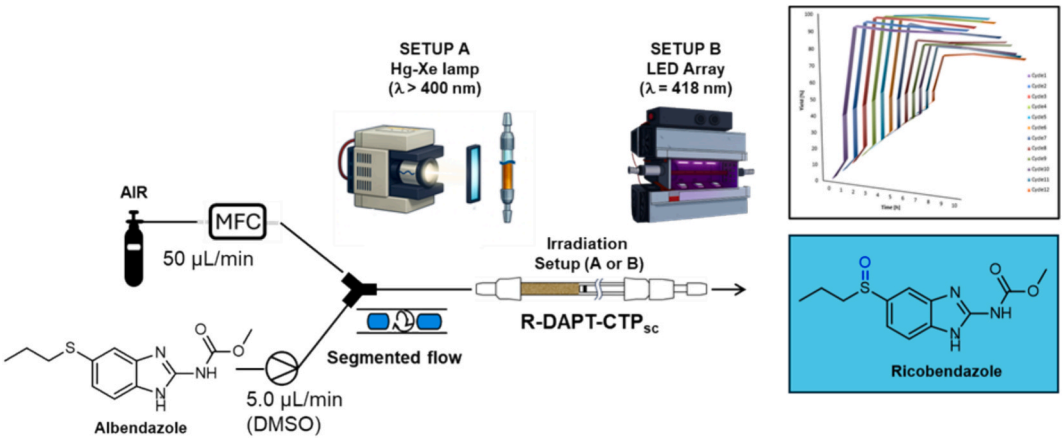

Fig. 8. Continuous-flow production of **Ricobendazole** using reactor **R-DAPT-CTP$_{sc}$**, with irradiation setups A and B, and long-term stability study.

formation of sulfone byproduct (<5%). Next, we aimed to further improve process productivity by halving the catalyst (150 mg) inside the reactor **R$_2$-DAPT-CTP$_{sc}$** and enhancing irradiation efficiency. For this purpose, a custom-made irradiation system (Fig. 8, Setup B), displaying a 60 W LED array (6 LEDs, 10 W each, λ = 418 nm), was assembled, guaranteeing powerful effective irradiation of the entire column. Preliminary studies conducted with the novel but unoptimized setup clearly showed the predominant formation of an undesired byproduct, derived from the cleavage of the carbamic group of **Albendazole** [59], which caused reactor clogging.

We wondered about the rationale behind the formation of the byproduct, and we assumed that it could be ascribed to a thermal effect, considering the measured high temperature of the reactor liquid outstream (>90 °C). Therefore, we decided to upgrade the photoreactor system introducing two additional fans frontward and backward to the column (Fig. S20c, Supporting Information), guaranteeing an efficient cooling of the reaction mixture (outstream liquid temperature ≤35 °C). To our delight, working under the optimized conditions, the steady state was achieved after 120 min, further increasing **Ricobendazole** yield to 93%, without detecting the formation of the undesired byproduct. Strikingly, the reactor could be operated for 50 h (5 consecutive runs of 10 h each) without any substantial loss in production efficiency. After this period, a progressive yield decrease was observed, recording after 120 h of total operation a loss of only half the initial productivity (Fig. 8).

3. Conclusions

In summary, we have successfully synthesized diamino-*p*-terphenyl covalent triazine polymers (**DAPT-CTPs**) by the highly efficient nucleophilic substitution polymerization strategy. Following a detailed morphological, optical, electrochemical, and photophysical characterization using various experimental techniques and DFT calculations, **DAPT-CTPs** were effectively tested in the visible-light generation of ROS to promote selective sulfide-to-sulfoxide aerobic oxidations and cross-dehydrogenative couplings, demonstrating the versatility of the designed photoactive material. The high stability of **DAPT-CTPs** was evidenced in recycling batch experiments and further confirmed by its utilization as packing material for the fabrication of fixed-bed photoreactors, which could be operated in continuous-flow mode for ca. two days to produce a target active pharmaceutical ingredient. The implementation of **DAPT-CTP** materials in CO_2 utilization processes is currently underway in our laboratories, and results will be reported in due course.

CRediT authorship contribution statement

Andrea Odoardo: Writing – original draft, Investigation. **Martina Milani:** Investigation. **Alessandra Molinari:** Writing – original draft, Investigation. **Lorenzo Poletti:** Investigation. **Carmela De Risi:** Writing – review & editing. **Stefano Caramori:** Writing – original draft, Supervision, Methodology. **Carmine D'Agostino:** Writing – review & editing. **Min Hu:** Writing – original draft, Investigation. **Paolo Dambruoso:** Investigation. **Daniele Cortecchia:** Investigation. **Graziano Di Carmine:** Writing – review & editing, Funding acquisition. **Daniele Ragno:** Writing – review & editing, Writing – original draft, Supervision, Methodology, Funding acquisition, Conceptualization. **Alessandro Massi:** Writing – review & editing, Writing – original draft, Supervision, Methodology, Funding acquisition, Conceptualization.

Declaration of competing interest

The authors declare that they have no known competing financial interests or personal relationships that could have appeared to influence the work reported in this paper.

Acknowledgements

A.M., D.R, and G.D.C acknowledge funding from the Italian Ministry of Education and Research (PRIN 2022, grant number: 2022JM3LZ3; PRIN 2022, grant number: 20225X2FS5; PRIN 2022 PNRR, grant number: P20224TTZF). D.C. acknowledges funding from the European Union's Horizon Europe Research Council program under Grant Agreement No. 101040681 (ERC Starting Grant SUPER). The authors acknowledge the use of the instruments at the Electron Microscopy Center of the University of Ferrara and the scientific and technical assistance of Paola Boldrini and Cinzia Brenna. Thanks are also given to Paolo Formaglio for NMR experiments and to Ercolina Bianchini for elemental analyses.

Appendix A. Supplementary material

Supplementary data contain: general experimental conditions, optical and photoelectrochemical properties of **DAPT-CTPs**, calculation methods, procedures for the synthesis and characterization of **DAPT-CTP** catalysts, sulfoxides **2**, sulfones **3**, aryl glycines **4**, indole **5g**, NPAAs **6** and **Ricobendazole**. Recycle experiments, quenching experiments and selective sulfide oxidation in continuous-flow. Performance comparison with reported catalysts. NMR spectra of **DAPT-CTP**, sulfoxides **2**, sulfones **3**, aryl glycines **4**, indole **5g** and NPAAs **6** and **Ricobendazole**.

Appendix B. Supplementary data

Supplementary data to this article can be found online at https://doi.org/10.1016/j.jcat.2026.116984.

Data availability

Data will be made available on request.

References

[1] B. Han, Porous organic polymers, J. Polym. Sci. 62 (8) (2024) 1491–1492, https://doi.org/10.1002/pol.20240193.

[2] S. Das, P. Heasman, T. Ben, S. Qiu, Porous organic materials: strategic design and structure–function correlation, Chem. Rev. 117 (3) (2017) 1515–1563, https://doi.org/10.1021/acs.chemrev.6b00439.

[3] F. Chen, H. Zheng, Y. Yusran, H. Li, S. Qiu, Q. Fang, Exploring high-connectivity three-dimensional covalent organic frameworks: topologies, structures, and emerging applications, Chem. Soc. Rev. 54 (1) (2025) 484–514, https://doi.org/10.1039/D4CS00703D.

[4] W. Song, Y. Tang, B.Y. Moon, Q. Liao, H. Xu, Q. Hou, H. Zhang, D.-G. Yu, Y. Liao, I. Kim, Green synthesis of hypercrosslinked polymers for CO2 capture and conversion: recent advances, opportunities, and challenges, Green Chem. 26 (5) (2024) 2476–2504, https://doi.org/10.1039/D3GC04222G.

[5] H. Ali, O. Iqbal, M. Sadiq, Y. Cheng, X. Yan, B. Al Alwan, A. El Jery, H. Rahman, Y. ur Qian, A. Hayat, D. Yue, Z. Ajmal, Novel advancements in synthesis, modulation, and potential applications of conjugated microporous polymer-based materials, Nano Mater. Sci. (2025), https://doi.org/10.1016/j.nanoms.2024.08.008.

[6] Y. Tian, G. Zhu, Porous Aromatic Frameworks (PAFs), Chem. Rev. 120 (16) (2020) 8934–8986, https://doi.org/10.1021/acs.chemrev.9b00687.

[7] S. Aggarwal, S.K. Awasthi, Emerging trends in the development and applications of triazine-based covalent organic polymers: a comprehensive review, Dalton Trans. 53 (28) (2024) 11601–11643, https://doi.org/10.1039/D4DT01127A.

[8] S.E. Peter, P. Thomas, P. Vairavel, N.V. Anil Kumar, Cyanuric chloride as a linker towards the synthesis of covalent triazine polymers: a review, Mater. Adv. 5 (23) (2024) 9175–9209, https://doi.org/10.1039/D4MA00739E.

[9] Y. Ren, S. Yang, Y. Xu, Crystalline covalent triazine frameworks and 2D triazine polymers: synthesis and applications, Acc. Chem. Res. 58 (3) (2025) 474–487, https://doi.org/10.1021/acs.accounts.4c00729.

[10] M. Liu, L. Guo, S. Jin, B. Tan, Covalent triazine frameworks: synthesis and applications, J. Mater. Chem. A 7 (10) (2019) 5153–5172, https://doi.org/10.1039/C8TA12442F.

[11] H. Wang, Z. Wang, M. Li, W. Hou, Q. Wen, Y. Zhu, H. Peng, G. Ma, L. Zhu, I. Shakir, Y. Xu, Recent advances in synthesis of covalent triazine frameworks: methods, mechanism, and crystallization effects, Adv. Synth. Catal. 367 (19) (2025), https://doi.org/10.1002/adsc.70123.

[12] Subodh, K. Prakash, K. Chaudhary, D.T. Masram, A new triazine-cored covalent organic polymer for catalytic applications, Appl. Catal. A 593 (2020) 117411, https://doi.org/10.1016/j.apcata.2020.117411.

[13] D. Yadav, S.K. Awasthi, A Pd confined hierarchically conjugated covalent organic polymer for hydrogenation of nitroaromatics: catalysis, kinetics, Thermodyn. Mech. Green Chem. 22 (13) (2020) 4295–4303, https://doi.org/10.1039/D0GC01469A.

[14] A.A. Raza, S. Ravi, S.S. Tajudeen, A.K.I. Sheriff, Applications of covalent triazine polymers in catalytic organic transformations, Current Catalysis 10 (1) (2021) 42–74, https://doi.org/10.2174/2211544710666210210105039.

[15] Tadayoni, S. Nayereh, M. Dinari, A. Torbatian, Novel flower-like magnetic core-shell covalent triazine polymer as a beneficial direct scarlet 4BS adsorbent and comprehensive study of the kinetics and isotherm adsorption, J. Environ. Chem. Eng. 11 (5) (2023) 110647, https://doi.org/10.1016/j.jece.2023.110647.

[16] R. Zhao, C. Niu, M.F. Aly Aboud, I. Shakir, C. Yu, Y. Xu, Monomer-dependent synthesis of secondary amine-linked triazine-based two-dimensional polymers nanosheets, Sci. China Chem. 63 (7) (2020) 966–972, https://doi.org/10.1007/s11426-020-9720-1.

[17] W. Dai, Q. Li, J. Long, P. Mao, Y. Xu, L. Yang, J. Zou, X. Luo, Hierarchically mesoporous imidazole-functionalized covalent triazine framework: an efficient metal- and halogen-free heterogeneous catalyst towards the cycloaddition of CO2 with epoxides, J.CO2 Util. 62 (2022) 102101, https://doi.org/10.1016/j.jcou.2022.102101.

[18] W. Wang, Y. Yuan, F.-X. Sun, G.-S. Zhu, Targeted synthesis of novel porous aromatic frameworks with selective separation of CO2/CH4 and CO2/N2, Chin. Chem. Lett. 25 (11) (2014) 1407–1410, https://doi.org/10.1016/j.cclet.2014.08.002.

[19] C. Yang, S. Wan, B. Zhu, J. Yu, S. Cao, Calcination-regulated microstructures of donor-acceptor polymers towards enhanced and stable photocatalytic H2O2 production in pure water, Angew. Chem. Int. Ed. 61 (39) (2022), https://doi.org/10.1002/anie.202208438.

[20] Q. Zhang, J. Zhou, H. Zhang, C. Qi, Q. Zhou, R. Guo, H. Yang, T. Xing, M. Wang, M. Wu, W. Wu, Terphenyl functionalized covalent triazine polymer as metal-free photocatalyst for superior hydrogen peroxide production, Adv. Funct. 34 (32) (Mater 2024,), https://doi.org/10.1002/adfm.202401579.

[21] P. Puthiaraj, Y.-R. Lee, S. Zhang, W.-S. Ahn, Triazine-based covalent organic polymers: design, synthesis and applications in heterogeneous catalysis, J. Mater. Chem. A 4 (42) (2016) 16288–16311, https://doi.org/10.1039/C6TA06089G.

[22] Z. Qian, Z.J. Wang, K.A.I. Zhang, Covalent triazine frameworks as emerging heterogeneous photocatalysts, Chem. Mater. 33 (6) (2021) 1909–1926, https://doi.org/10.1021/acs.chemmater.0c04348.

[23] A. López-Magano, S. Daliran, A.R. Oveisi, R. Mas-Ballesté, A. Dhakshinamoorthy, J. Alemán, H. Garcia, R. Luque, Recent advances in the use of covalent organic frameworks as heterogenous photocatalysts in organic synthesis, Adv. Mater. 35 (24) (2023), https://doi.org/10.1002/adma.202209475.

[24] L. Poletti, D. Ragno, O. Bortolini, F. Presini, F. Pesciaioli, S. Carli, S. Caramori, A. Molinari, A. Massi, G. Di Carmine, Photoredox cross-dehydrogenative coupling of N-aryl glycines mediated by mesoporous graphitic carbon nitride: an environmentally friendly approach to the synthesis of non-proteinogenic α-amino acids (NPAAs) decorated with indoles, J. Org. Chem. 87 (12) (2022) 7826–7837, https://doi.org/10.1021/acs.joc.2c00474.

[25] Poletti, L.; Codecà, N.; Ragno, D.; Risi, C. De; Toldo, S.; Bortolini, O.; Shao, J.; An, L.; Lee, D.; D'Agostino, C.; Dambruoso, P.; Massi, A.; Carmine, G. Di. A Telescoped Photo-/Organo-Catalyzed Cross Dehydrogenative Coupling (CDC) between Glycine Derivatives and Ketones to Afford Nonproteinogenic Amino Acids (NPAAs) Enabled by Heterogeneous Continuous Flow Catalysis. ACS Sustain. Chem. Eng. 2024, 12 (41), 15193–15202. Doi: 10.1021/acssuschemeng.4c05931.

[26] P. Dambruoso, M. Ballestri, C. Ferroni, A. Guerrini, G. Sotgiu, G. Varchi, A. Massi, TPPS supported on core–shell PMMA nanoparticles: the development of continuous-flow membrane-mediated electrocoagulation as a photocatalyst processing method in aqueous media, Green Chem. 17 (3) (2015) 1907–1917, https://doi.org/10.1039/C4GC01996B.

[27] E. Block, The organosulfur chemistry of the genus allium– implications for the organic chemistry of sulfur, Angew. Chem. Int. Ed. 31 (9) (1992) 1135–1178, https://doi.org/10.1002/anie.199211351.

[28] E. Skolia, P.L. Gkizis, N.F. Nikitas, C.G. Kokotos, Photochemical aerobic oxidation of sulfides to sulfoxides: the crucial role of wavelength irradiation, Green Chem. 24 (10) (2022) 4108–4118, https://doi.org/10.1039/D2GC00799A.

[29] T. Tian, Z. Li, C.-J. Li, Cross-dehydrogenative coupling: a sustainable reaction for C–C bond formations, Green Chem. 23 (18) (2021) 6789–6862, https://doi.org/10.1039/D1GC01871J.

[30] Y. Ding, J.P. Ting, J. Liu, S. Al-Azzam, P. Pandya, S. Afshar, Impact of non-proteinogenic amino acids in the discovery and development of peptide therapeutics, Amino Acids 52 (9) (2020) 1207–1226, https://doi.org/10.1007/s00726-020-02890-9.

[31] Z. Wang, M. He, B. Chen, B. Hu, Triazine covalent organic polymer coated stir bar sorptive extraction coupled with high performance liquid chromatography for the analysis of trace phthalate esters in mineral water and liquor samples, J. Chromatogr. A 1660 (2021) 462665, https://doi.org/10.1016/j.chroma.2021.462665.

[32] P.R. Ogilby, Solvent effects on the radiative transitions of singlet oxygen, Acc. Chem. Res. 32 (6) (1999) 512–519, https://doi.org/10.1021/ar980005p.

[33] K. Wu, P.-W. Cheng, X.-Y. Liu, J. Zheng, X.-W. Zhu, M. Xie, P. Weng, W. Lu, D. Li, Polarization engineering in porous organic polymers for charge separation efficiency and its applications in photocatalytic aerobic oxidations, Sci. China Chem. 67 (3) (2024) 1000–1007, https://doi.org/10.1007/s11426-023-1820-5.

[34] Z. Lan, Y. Fang, Y. Zhang, X. Wang, Photocatalytic oxygen evolution from functional triazine-based polymers with tunable band structures, Angew. Chem. Int. Ed. 57 (2) (2018) 470–474, https://doi.org/10.1002/anie.201711155.

[35] Y. Zhou, W. Zhao, Synergistic effect of π-π and p-π conjugation of a commercial amine for enhanced photocatalytic CO2 cycloaddition reaction, Appl. Catal. A 698 (2025) 120249, https://doi.org/10.1016/j.apcata.2025.120249.

[36] K. Makino, T. Hagiwara, A. Murakami, A mini review: fundamental aspects of spin trapping with DMPO, Int. J. Radiat. Appl. Instrum. Part C 37 (5–6) (1991) 657–665, https://doi.org/10.1016/1359-0197(91)90164-W.

[37] Y. Nosaka, A.Y. Nosaka, Generation and detection of reactive oxygen species in photocatalysis, Chem. Rev. 117 (17) (2017) 11302–11336, https://doi.org/10.1021/acs.chemrev.7b00161.

[38] M.C. Carreno, Applications of sulfoxides to asymmetric synthesis of biologically active compounds, Chem. Rev. 95 (6) (1995) 1717–1760, https://doi.org/10.1021/cr00038a002.

[39] M. Feng, B. Tang, H.S. Liang, X. Jiang, Sulfur containing scaffolds in drugs: synthesis and application in medicinal chemistry, Curr. Top. Med. Chem. 16 (11) (2016) 1200–1216, https://doi.org/10.2174/1568026615666150915111741.

[40] P. Devendar, G.-F. Yang, Sulfur-containing agrochemicals, Top. Curr. Chem. 375 (6) (2017) 82, https://doi.org/10.1007/s41061-017-0169-9.

[41] X. Xu, X. Huang, Y. Chang, Y. Yu, J. Zhao, N. Isahak, J. Teng, R. Qiao, H. Peng, C.-X. Zhao, T.P. Davis, C. Fu, A.K. Whittaker, Antifouling surfaces enabled by surface grafting of highly hydrophilic sulfoxide polymer brushes, Biomacromolecules 22 (2) (2021) 330–339, https://doi.org/10.1021/acs.biomac.0c01193.

[42] E. Skolia, P.L. Gkizis, C.G. Kokotos, Aerobic photocatalysis: oxidation of sulfides to sulfoxides, ChemPlusChem 87 (4) (2022), https://doi.org/10.1002/cplu.202200008.

[43] J. Chen, W. Sun, Y. Zhao, Green molecular reactor boosting the photocatalytic aerobic oxidation of sulfides in clean solvent, ChemCatChem 16 (20) (2024), https://doi.org/10.1002/cctc.202400840.

[44] S.M. Bonesi, S. Crespi, D. Merli, I. Manet, A. Albini, Direct irradiaton of aryl sulfides: homolytic fragmentation and sensitized S-oxidation, J. Org. Chem. 82 (17) (2017) 9054–9065, https://doi.org/10.1021/acs.joc.7b01518.

[45] C. Schoeneich, A. Aced, K.D. Asmus, Mechanism of oxidation of aliphatic thioethers to sulfoxides by hydroxyl radicals. The importance of molecular oxygen,

J. Am. Chem. Soc. 115 (24) (1993) 11376–11383, https://doi.org/10.1021/ja00077a042.
[46] C. Ni, W. Chen, C. Jiang, H. Lu, Visible light-induced aerobic oxidative cross-coupling reaction: preparation of α-indolyl glycine derivatives, New J. Chem. 44 (2) (2020) 313–316, https://doi.org/10.1039/C9NJ05211A.
[47] S. Zhu, M. Rueping, Merging visible-light photoredox and lewis acid catalysis for the functionalization and arylation of glycine derivatives and peptides, Chem. Comm. 48 (98) (2012) 11960, https://doi.org/10.1039/c2cc36995h.
[48] J.H. Kim, H. Yun, D.W. Kang, J. Shin, M. Kang, N. Singh, J.-E. Jeong, C.S. Hong, J. S. Kim, Isomeric Sp2-C-conjugated porous organic polymer-mediated photo- and sono-catalytic detoxification of sulfur mustard simulant under ambient conditions, Matter 4 (11) (2021) 3774–3785, https://doi.org/10.1016/j.matt.2021.10.005.
[49] E.L. Clennan, Persulfoxide: key intermediate in reactions of singlet oxygen with sulfides, Acc. Chem. Res. 34 (11) (2001) 875–884, https://doi.org/10.1021/ar0100879.
[50] Z.-H. Long, D. Luo, K. Wu, Z.-Y. Chen, M.-M. Wu, X.-P. Zhou, D. Li, Superoxide ion and singlet oxygen photogenerated by metalloporphyrin-based metal–organic frameworks for highly efficient and selective photooxidation of a sulfur mustard simulant, ACS Appl. Mater. Interfaces 13 (31) (2021) 37102–37110, https://doi.org/10.1021/acsami.1c08840.
[51] Q. Li, X. Lan, G. An, L. Ricardez-Sandoval, Z. Wang, G. Bai, Visible-light-responsive anthraquinone functionalized covalent organic frameworks for metal-free selective oxidation of sulfides: effects of morphology and structure, ACS Catal. 10 (12) (2020) 6664–6675, https://doi.org/10.1021/acscatal.0c00290.
[52] F. Parrino, S. Livraghi, E. Giamello, R. Ceccato, L. Palmisano, Role of hydroxyl, superoxide, and nitrate radicals on the fate of bromide ions in photocatalytic TiO_2 suspensions, ACS Catal. 10 (14) (2020) 7922–7931, https://doi.org/10.1021/acscatal.0c02010.
[53] Y. Zhang, J. Pang, J. Li, X. Yang, M. Feng, P. Cai, H.-C. Zhou, Visible-light harvesting pyrene-based MOFs as efficient ROS generators, Chem. Sci. 10 (36) (2019) 8455–8460, https://doi.org/10.1039/C9SC03080H.
[54] S.-S. Zhu, L. Zuo, Y. Liu, B. Yu, 1,2,3,5-Tetrakis(carbazol-9-Yl)-4,6-dicyanobenzene (4CzIPN)-based porous organic polymers for visible-light-driven organic transformations in water under aerobic oxidation, Green Chem. 24 (22) (2022) 8725–8732, https://doi.org/10.1039/D2GC02950B.
[55] Z. Ma, S. Liu, N. Tang, T. Song, K. Motokura, Z. Shen, Y. Yang, Coexistence of Fe nanoclusters boosting fe single atoms to generate singlet oxygen for efficient aerobic oxidation of primary amines to imines, ACS Catal. 12 (9) (2022) 5595–5604, https://doi.org/10.1021/acscatal.1c04467.
[56] C.E. Lanusse, G.L. Virkel, S.F. Sanchez, L.I. Alvarez, A.L. Lifschitz, F. Imperiale, A. Monfrinotti, Ricobendazole kinetics and availability following subcutaneous administration of a novel injectable formulation to calves, Res. Vet. Sci. 65 (1) (1998) 5–10, https://doi.org/10.1016/S0034-5288(98)90019-4.
[57] V. Králová, V. Hanušová, P. Staňková, K. Knoppová, K. Čáňová, L. Skálová, Antiproliferative effect of benzimidazole anthelmintics albendazole, ricobendazole, and flubendazole in intestinal cancer cell lines, Anticancer Drugs 24 (9) (2013) 911–919, https://doi.org/10.1097/CAD.0b013e3283648c69.
[58] G. Di Carmine, C. D'Agostino, O. Bortolini, L. Poletti, C. De Risi, D. Ragno, A. Massi, Heterogeneous organocatalysts for light-driven reactions in continuous flow, Molecules 29 (10) (2024) 2166, https://doi.org/10.3390/molecules29102166.
[59] M. Noshita, Y. Shimizu, H. Morimoto, T. Ohshima, Diethylenetriamine-Mediated Direct Cleavage of Unactivated Carbamates and Ureas, Org. Lett. 18 (23) (2016) 6062–6065, https://doi.org/10.1021/acs.orglett.6b03016.